PHYSICAL REVIEW E **100**, 033111 (2019)

Numerical investigation of adhesion dynamics of a deformable cell pair on an adhesive substrate in shear flow

Ziying Zhang,[1,2] Jun Du,[1] Zhengying Wei,[1,*] Zhen Chen,[2] Chang Shu,[2,†] Zhen Wang,[3] and Minghui Li[3]
[1]*School of Mechanical Engineering, Xi'an Jiaotong University, Xi'an 710049, People's Republic of China*
[2]*Department of Mechanical Engineering, National University of Singapore, 10 Kent Ridge Crescent, Singapore 119260, Singapore*
[3]*Department of Orthopaedic Oncology, Xi-Jing Hospital, Air Force Military Medical University, Xi'an 710032, People's Republic of China*

(Received 19 February 2019; published 19 September 2019)

Adhesion dynamics of cells is of great value to biological systems and adhesion-based biomedical applications. Although adhesion of a single cell or capsule has been widely studied, physical insights into the adhesion dynamics of aggregates containing two or more cells remain elusive. In this paper, we numerically investigate the dynamic adhesion of a deformable cell pair to a flat substrate under shear flow. Specifically, the immersed boundary–lattice Boltzmann method is utilized as the flow solver, and the stochastic receptor-ligand kinetics model is implemented to recover cell-substrate and cell-cell adhesive interactions. Special attention is paid to the roles of the cell deformability and adhesion strengths in cellular motion. Four distinct adhesion states, namely, rolling, tumbling, firm adhesion, and detachment, are identified and presented in phase diagrams as a function of the adhesion strengths for cell pairs with different deformabilities. The simulation results suggest that both the cell-cell and cell-substrate adhesion strengths act as the resistance to the rolling motion, and dominate the transition among various adhesion states. The cell deformability not only enhances the resistance effect, but also contributes to detachment or fast tumbling of the cell pair. These findings enrich the understanding of adhesion dynamics of cell aggregates, which could shed light on complex adhesion processes and provide instructions in developing adhesion-based applications.

DOI: 10.1103/PhysRevE.100.033111

I. INTRODUCTION

Cell adhesion is of fundamental importance in many physiological processes, including immune response, hemostatic plug formation, and stem cell homing [1–3]. Adherent cells (e.g., leukocytes, thrombocytes, and stem cells) may exhibit different mechanical properties and various expressions of adhesion molecules, which yields distinct adhesion capacity and characteristics. In biomedical applications, by utilizing the adhesion characteristics of specific cells, adhesion-based microfluidics has been developed to manipulate and sort the target cells [4–6]. Specific adhesion states of the cells are physical outcomes of the delicate balance between the adhesive forces and the hydrodynamic forces under certain physiological and physical conditions. Therefore, investigations into the complex interplay among the imposed flow, cells, and adhesive interactions would be valuable for understanding the adhesion mechanisms.

Plenty of work has been carried out both experimentally and numerically to provide insights into adhesion dynamics of a single cell [7,8]. Cell adhesion is mainly regulated by molecular bonding between cell-surface receptors and their ligands in the external environment or counter-receptors on other cells, and the associated adhesive interactions can be numerically interpreted by various models like the Morse potential model [9,10], the deterministic model [11,12], and the probabilistic model [13,14]. First proposed by Hammer and Apte, the stochastic receptor-ligand binding kinetic was proven to be a faithful numerical approach to understanding the dynamics of leukocyte adhesion [13]. Continuous efforts have been made then to enrich its applicability to different cell types (e.g., red blood cells, platelets, and tumor cells), deformable capsules, and other adhesive interactions [15–19]. In particular, the near-wall adhesion dynamics is affected by both the flow shear rate and the molecular properties of adhesion bonds (e.g., bond elasticity, association and dissociation rates, receptor and ligand densities, etc.) [20–22]. Besides, hydrodynamics of the thin fluid layer between the cell-cell or cell-substrate surfaces was shown to be influential to the separation distance and the adhesion dynamics [23,24], indicating the importance of cellular protrusions in receptor-ligand proximity [25]. Moreover, some recent studies indicated that increasing the cell deformability enlarges the cell-substrate contact area and thus reduces the rolling velocity [14,17,26], which in turn affects transitions among various adhesion states such as rolling, firm-adhesion, and detachment [12,27]. Typical transitions of crawling-to-flipping and flipping-to-rolling were observed for malaria-infected RBCs owing to the cell stiffening and shape change [19,28].

In blood circulation or imposed fluid within microfluidics, cells may migrate as individuals, but may also move collectively as chains or clusters. The adhesion of cell aggregates to the vascular endothelium is vital in many important physiological processes. For example, the aggregation of platelets plays a particular role in hemostatic and thrombotic processes [2]; circulating tumor cell (CTC) clusters possess

---

[*] zywei@mail.xjtu.edu.cn
[†] mpeshuc@nus.edu.sg

much greater metastatic potential and efficiency of seeding colonies than individual CTCs [29,30]. These phenomena raise the question of how the adhesion behavior of aggregates containing two or more cells differs from the motion of a single cell. Initial works on this topic usually simplified the cells into particles and thus neglected the adhesive forces among them. The studies were then focused on the collision and crossing processes in shear flow, aiming to explain the influences of flow rate, inertia, particle deformation, and initial separation distance on the pairwise interaction [31–34]. King and Hammer considered the adhesion between multiple isolated rigid particles and a surface in Couette flow; they found that increasing particle proximity reduces the rolling velocity [35]. More recently, some interesting progress was made on the topic by considering the deformation of cells. Alexeev *et al.* investigated approaching and separation motions of two deformable capsules and noticed that such motion depends on substrate compliance, capsule elasticity, and the adhesion strength to the substrate [10]. The aggregation and dissociation of multiple cells in shear flow were studied by Zhang *et al.* [36], and the dynamic behaviors of the aggregate were shown to be related to the strength of intercellular adhesion. Gupta *et al.* further incorporated the stochastic receptor-ligand binding kinetics for the cell-cell interactions, to investigate the adhesion and detachment between two deformable cells under pulling forces [37]. These studies emphasize the interactions among cells in the free stream. Nevertheless, investigations into the dynamics of aggregated cells in the context of near-wall adhesion remain scarce.

In this work, in order to arrive at a generic scenario, we consider an aggregate of two deformable cells which initially adheres to the vessel wall (i.e., an adhesive substrate), and numerically investigate the adhesion dynamics of the cell pair under linear shear flow. The immersed boundary–lattice Boltzmann method is utilized as the flow solver [27,38], while the stochastic receptor-ligand kinetics [13] is incorporated to recover the cell-to-cell and cell-to-substrate adhesive interactions. By varying the adhesion strength or the cell deformability, four distinct adhesion states, namely, rolling, tumbling, firm adhesion, and detachment, are identified, and phase diagrams for these states are established. The study described herein presents simulations for the dynamic adhesion of multiple deformable cells with the interactions of cell-cell and cell-wall stochastic bonds binding under imposed flow.

The remaining parts of this paper are organized as follows. A brief description of the computational framework and the numerical setup are included in Sec. II. Section III presents the simulation results and detailed discussions of the dynamics of the cell pair near the adhesive wall and exposed in the shear flow. Conclusions are finally drawn in Sec. IV.

II. METHODOLOGY

A. Problem definition

The physical configuration of the present problem is illustrated in Fig. 1. The cell is defined as a deformable capsule enclosed by an isotropic hyperelastic membrane. Two identical cells having an equilibrium spherical shape with a radius R are placed near the bottom wall. The two cells are in close proximity and range along the flow direction. A linear shear flow with a shear rate of $\dot{\gamma}$ is induced by the moving top wall. Internal and external fluids of the cell are assumed to be Newtonian and incompressible with the same density ρ and viscosity ν. It should be noted that the cytoplasmic viscosity of the cell is usually larger than the ambient fluid. The effect of the cytoplasmic viscosity on cell adhesion can be found in the study of Khismatullin and Truskey [39], in which cell deformability is modulated by the viscosity. In the present study, the effect of the viscosity ratio is not considered, and membrane elasticity plays a dominant role in determining cell deformability. With regard to adhesive interactions between the surfaces, cell-to-wall and cell-to-cell adhesions are mediated by specific binding between cell receptors and their counterparts on the substrate or the other cell. The receptors are located on the tips of cellular protrusions, such as microvilli of leukocytes and knobs of malaria-infected erythrocytes, which are of significance to bring the adhesion molecules to sufficient proximity for binding [25,40]. As the adhesion bond is linked and stretched, a pulling force is generated and applied on the protrusions. For simplicity, the protrusions are treated as massless rigid cylinders which only transmit forces but have no influence on the fluid field.

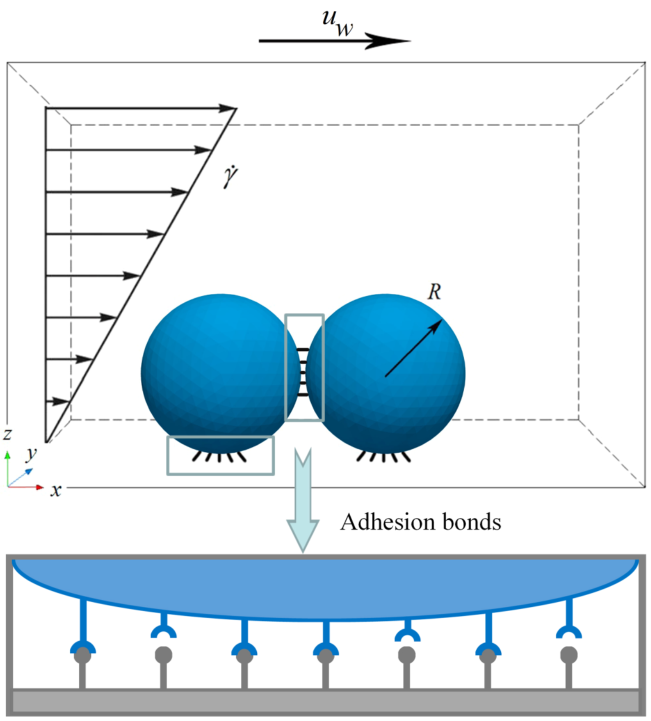

FIG. 1. Schematic illustration of the adhesion of a cell pair in shear flow. The deformable cells are initially in the shape of a sphere with the radius R, in tandem arrangement along the flow direction. The linear shear flow (shear rate $\dot{\gamma}$) is generated by assigning the top wall with a constant velocity of u_w. Cell-cell and cell-substrate adhesive interactions are mediated by the binding of adhesion bonds with the probabilistic rule.

The proposed problem will be numerically investigated in this paper. Specifically, the lattice Boltzmann method serves as the flow solver, in which the immersed boundary method is implemented to cast the boundary effect of the cell membrane.

A constitutive energy model consisting of strain, bending, surface, and volume constraints is used to govern the elastic mechanics of the membrane; the finite-element method is employed to solve the constitutive equation. The adhesive interactions are modeled by the stochastic receptor-ligand binding kinetics. Details and validation of the present model can be found in our previous studies [27,41]. Here, only a brief outline of the numerical methods is given as follows.

B. Immersed boundary–lattice Boltzmann method

The multiple-relaxation-time lattice Boltzmann equation (MRT-LBE) with force term is used to govern the fluid flow [42,43],

$$f_i(\boldsymbol{x}+\boldsymbol{e}_i\Delta t, t+\Delta t) - f_i(\boldsymbol{x},t) = \Omega_i(\boldsymbol{x},t)\Delta t + F_i(\boldsymbol{x},t)\Delta t, \tag{1}$$

$$\boldsymbol{\Omega}(\boldsymbol{x},t) = -\mathbf{M}^{-1}\mathbf{S}[\mathbf{m}(\boldsymbol{x},t) - \mathbf{m}^{(\mathrm{eq})}(\boldsymbol{x},t)]. \tag{2}$$

The particle distribution functions f_i are transformed into the velocity moments $\mathbf{m}$ for the collision via $\mathbf{m} = \mathbf{M}\cdot\mathbf{f}$; $\mathbf{m}^{(\mathrm{eq})}$ is the equilibrium value of the velocity moments; $\mathbf{S}$ represents a diagonal relaxation matrix consisting of the relaxation parameters. The external force term F_i incorporates the effect of body force $\bar{\boldsymbol{f}}$ into Eq. (1) by

$$\boldsymbol{F}(\boldsymbol{x},t) = \mathbf{M}^{-1}\left(I - \frac{1}{2}\mathbf{S}\right)\mathbf{M}\bar{\boldsymbol{F}}(\boldsymbol{x},t), \tag{3}$$

$$\bar{\boldsymbol{F}}(\boldsymbol{x},t) = \omega_i\left[\frac{\boldsymbol{e}_i - \boldsymbol{u}(\boldsymbol{x},t)}{c_s^2} + \frac{\boldsymbol{e}_i\cdot\boldsymbol{u}(\boldsymbol{x},t)}{c_s^4}\boldsymbol{e}_i\right]\cdot\bar{\boldsymbol{f}}(\boldsymbol{x},t), \tag{4}$$

where $\boldsymbol{e}_i$ represents the 19 lattice velocity vectors for the D3Q19 model, ω_i $(i = 0, 1, \dots, 18)$ is the weight coefficient, and $c_s = \sqrt{1/3}\Delta x/\Delta t$ is the sound speed. The macroscopic density and velocity can be obtained from

$$\rho = \sum_i f_i, \quad \rho\boldsymbol{u} = \sum_i f_i\boldsymbol{e}_i + \frac{\Delta t}{2}\bar{\boldsymbol{f}}. \tag{5}$$

The shear flow is induced by moving the top wall with a velocity $\boldsymbol{u}_w$, which can be realized by the halfway bounce-back method [44],

$$f_{i'}(\boldsymbol{x},t+1) = f_i^*(\boldsymbol{x},t) - 2\omega_i\rho\frac{\boldsymbol{u}_w\cdot\boldsymbol{e}_i}{c_s^2}, \tag{6}$$

where i' denotes the velocity direction opposite to i, i.e., $\boldsymbol{e}_{i'} = -\boldsymbol{e}_i$, and $f_i^*(\boldsymbol{x},t)$ is the postcollision distribution function. Stationary walls are applied by setting $\boldsymbol{u}_w = 0$.

The immersed boundary method (IBM) is employed to pose the effect of the deformable moving boundary of the cell membrane on the flow field. In IBM, fluid-membrane interaction is explicitly coupled through the spreading and interpolation equations [45],

$$\bar{\boldsymbol{f}}(\boldsymbol{x},t) = \int \mathbf{F}(\boldsymbol{s},t)\delta[\boldsymbol{x} - \mathbf{X}(\boldsymbol{s},t)]d\boldsymbol{s}, \tag{7}$$

$$\mathbf{U}(\boldsymbol{s},t) = \int \boldsymbol{u}(\boldsymbol{x},t)\delta[\boldsymbol{x} - \mathbf{X}(\boldsymbol{s},t)]d\boldsymbol{x}, \tag{8}$$

where $\mathbf{X}$, $\mathbf{F}$, and $\mathbf{U}$ denote the Lagrangian coordinates, boundary force density, and velocity of the membrane nodes, respectively. The Dirac delta function $\delta(\boldsymbol{r}) = \phi(x)\phi(y)\phi(z)$ can be discretized by several interpolation functions ϕ with different ranges [45]. The finite range of the interpolations would introduce interface thickness and thus increase the hydrodynamic radius of the cell [38]. Thus, the linear interpolation function is adopted to have a small thickness of the numerical interface,

$$\phi(r) = \begin{cases} 1 - |r| & 0 \leqslant |r| \leqslant 1 \\ 0 & 1 \leqslant |r| \end{cases}. \tag{9}$$

The locations of the Lagrangian points on the membrane are updated through the second-order Adams-Bashforth scheme,

$$\mathbf{X}(\boldsymbol{s},t+\Delta t) = \mathbf{X}(\boldsymbol{s},t) + \left[\tfrac{3}{2}\mathbf{U}(\boldsymbol{s},t) - \tfrac{1}{2}\mathbf{U}(\boldsymbol{s},t-\Delta t)\right]\Delta t. \tag{10}$$

C. Cell model

The membrane of the cell is assumed to be a very thin shell, which is considered as a two-dimensional structure immersed in the three-dimensional fluid. A subdivision procedure similar to Ramanujan and Pozrikidis [46] is used to homogeneously generate the triangular meshes on the spherical membrane. The fluid forces imposed on the membrane yield its deformation and thus generate restoring forces towards the equilibrium state. The deformation of the cell membrane can be interpreted from the perspective of energy, which gives the following constitutive energy model [47]:

$$W = W_S + W_B + W_{A+V}, \tag{11}$$

where W_S, W_B, and W_{A+V} denote the strain energy, bending energy, and constraints on the cell surface area and volume, respectively. In this study, the two-dimensional Mooney-Rivlin law is employed for the strain energy term W_S,

$$W_S = \frac{K_S}{2}\int\left[\Psi\left(I_1 + 2 + \frac{1}{I_2+1}\right) + (1-\Psi)\left(\frac{I_1+2}{I_2+1} + I_2 + 1\right)\right]dA, \tag{12}$$

where I_1 and I_2 are the strain invariants relating to the local membrane deformation tensor, and Ψ is a constant coefficient. K_S denotes the surface shear modulus, and the surface elastic modulus is $E_S = 3K_S$ [48]. Deviations of the deformed angle θ between two adjacent face elements from the equilibrium angle θ^{eq} are constrained by the bending energy

$$W_B = K_B\int[1 - \cos(\theta - \theta^{eq})]\mathrm{d}A. \tag{13}$$

The value of the bending modulus with the fixed ratio $K_B/R^2K_S = 0.02$ is used to avoid buckling or collapse of the membrane in case of strong local curvature while maintaining negligible effects on the overall cell deformation [27,49]. Finally, constraints on the total surface area A and volume V of the cell are imposed by the energy term

$$W_{A+V} = \frac{K_A}{2}\frac{(A - A^{eq})^2}{A^{eq}} + \frac{K_V}{2}\frac{(V - V^{eq})^2}{V^{eq}}, \tag{14}$$

where A^{eq} and V^{eq} are the equilibrium surface area and equilibrium volume, respectively. The moduli $K_A = 0.05$ and $K_V = 0.05$ are used to ensure small deviations of the membrane surface and cytosol volume. As the energy of the membrane is obtained according to the deformation, the forces **F** on the discrete membrane nodes are calculated with the principle of virtual work.

As for the adhesive interactions, bond binding between receptors and their counterparts is governed by the stochastic binding kinetics. The adhesion force F_b generated from a stressed bond is modeled as a linear spring [13,50],

$$F_b = \sigma(x_m - \lambda), \tag{15}$$

where σ is the elastic constant, λ is the equilibrium bond length, and x_m is the length of the stretched bond. To model the stochastic nature of receptor-ligand interactions, forming and breaking of the bonds are governed by the association probability $P_f = 1 - \exp(-k_f \Delta t)$ and dissociation probability $P_r = 1 - \exp(-k_r \Delta t)$. The forward reaction rate k_f and reverse reaction rate k_r are, respectively, defined as [13,51]

$$k_f = k_f^0 \exp\left[-\frac{\sigma_{ts}(x_m - \lambda)^2}{2k_bT}\right], \tag{16}$$

and

$$k_r = k_r^0 \exp\left[-\frac{(\sigma - \sigma_{ts})(x_m - \lambda)^2}{2k_bT}\right], \tag{17}$$

where k_f^0 and k_r^0 are the unstressed association and dissociation rates, respectively; k_b is the Boltzmann constant; T is the absolute temperature. The transition state elastic constant σ_{ts} regulates the transition between "slip" bonds and "catch" bonds. As a slip bond ($\sigma > \sigma_{ts}$), its lifetime decreases with the increase of the applied force; it is called the catch bond ($\sigma < \sigma_{ts}$) if the bond lifetime is prolonged by the force, which was only observed for weak forces [50,52]. Since the applied shear flow in this study is sufficiently strong, we set $\sigma_{ts} = 0.02\sigma$ for the case of slip bonds [27,39].

The binding state of the bond is checked at each time step during the simulation. An existing formed bond is ruptured if the bond length x_m exceeds a reactive distance d_r or the calculated probability P_r is greater than a random number generated between 0 and 1. Similarly, within the reactive distance, a bond may be formed in terms of the association probability. Note that both the cell-cell and cell-substrate adhesive interactions are modeled by the above binding kinetics.

It is also suggested that, in order to prevent membrane-membrane and membrane-substrate overlap, a short-range repulsive force [27,47] should be applied on the membrane nodes when the distance between the nearby membranes or the distance between the membrane and wall falls within a cutoff distance. Physically, this repulsive force could arise from the compressing of the protrusions. In our implementations, the normal cutoff distance to the wall is $0.5\Delta x$, and the cutoff value is $1.8\Delta x$ for the membrane nodes. The short-range repulsive force maintains at least one layer of fluid nodes between the surfaces while it has no effect on the adhesive binding. We note that the lubrication hydrodynamics in the gap between the surfaces could affect membrane motion and receptor-ligand binding [23–25]. To capture such effect, in future work, higher resolution is necessary to more accurately resolve the fluid flow in the gap, and alternatively, lubrication correction could be introduced [53].

D. Simulation parameters

The computational fluid domain is $12R \times 8R \times 8R$ with periodic boundary condition implemented in the x and y directions. The shear flow is induced by the moving top wall along the x direction with velocity u_w, leading to an average shear rate of $\dot{\gamma} = u_w/8R$. The initial setup of the cell is a sphere with the radius of $R = 8\Delta x$, and the lattice constant Δx is equal to $0.5\,\mu$m. The cell membrane is represented by a finite-element mesh consisting of 1620 flat triangular elements and 812 nodes, which is obtained from the subdivision of a regular icosahedron. The protrusions are set with the length of the microvilli being $0.5\,\mu$m [13,39] and distributed on each membrane node, giving a total number of $N_m = 812$ on one cell [13,54]. Although usually there are several receptors on the tip, only one bond is allowed to be formed in the simulation to represent the binding of the receptor site. The ligand sites on the substrate are uniformly distributed on square lattices at a distance of $0.25\,\mu$m, corresponding to a density of $16/\mu\text{m}^2$ [55]. The maximum reactive distance for receptor-ligand bonding is set to $d_r = 300$ nm with an equilibrium bond length of 100 nm [56]. To have initial binding, the two cells are placed with the membrane $0.5\,\mu$m away from the substrate and $1\,\mu$m away from each other; in this case, several initial bonds (more than 20 are within the reaction distance) could be formed between the surfaces according to the association rate.

The dimensionless parameters that have significant impacts on adhesion behaviors of a single cell or capsule involve the capillary number $\text{Ca} = \rho\nu R\dot{\gamma}/E_S$, cell-substrate adhesion strength $\Gamma_s = \sigma_s/\rho\nu R\dot{\gamma}$, on rate $K_{\text{on}} = k_f^0/\dot{\gamma}$ and off rate $K_{\text{off}} = k_r^0/\dot{\gamma}$ [12,22,27]. To characterize the effect of the adhesion force between the cells, the intercellular adhesion strength is defined as $\Gamma_c = \sigma_c/\rho\nu R\dot{\gamma}$. In the limit of small Reynolds number ($\text{Re} \leqslant 0.1$, defined as $\text{Re} = R^2\dot{\gamma}/\nu$), inertia effects can be neglected and the effect of Re on deformation and adhesion of the cell is negligible [27,38]; that is, the exact value of Re is irrelevant within this range. Therefore, the Reynolds number is set to 0.05 in all subsequent simulations for shorter simulation time. In the present study, we mainly focus on the effects of cell deformability (Ca) and the adhesion strengths (Γ_s and Γ_c) on cell pair adhesion dynamics. The reaction rates $K_{\text{on}} = 1$ and $K_{\text{off}} = 0.1$ are chosen for cell-substrate binding; in this case, a single cell would exhibit rolling adhesion under the shear flow [20,22]. Note that the same parameters are used for the cell-cell and cell-substrate bonds except the adhesion strengths. With the shear rate $\dot{\gamma}$ fixed, Γ_s, Γ_c, and Ca are varied by varying the bond elastic constants (σ_s and σ_c) and the surface shear modulus K_S, respectively. Considering the randomness of the adhesion model, six independent simulation runs are performed for each case. Each simulation contributes to the mean values of motion characteristics and their standard deviations.

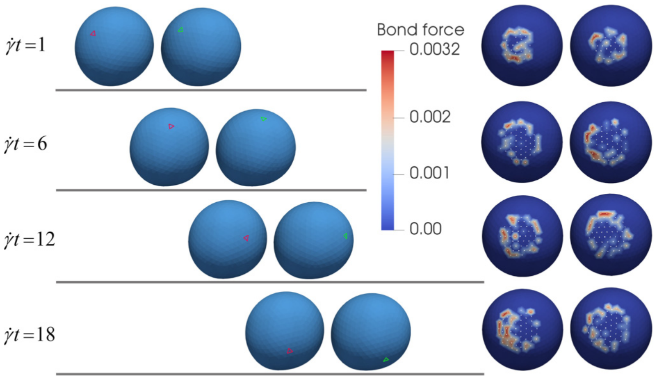

FIG. 2. Simulation snapshots of a cell pair presenting the rolling adhesion state at Ca = 0.002, $\Gamma_s = 50$, and $\Gamma_c = 50$. The *left column* is the side view. A triangular element of each cell is marked as the tracker of the cell motion, red for the *rear cell* and green (light gray) for the *front cell*. The *right column* shows the bottom shape and bond forces (in lattice units) acting on the membrane, and the linked protrusions are marked with white nodes.

III. RESULTS AND DISCUSSIONS

A. Adhesion states of the cell pair

By varying the parameters Ca, Γ_s, and Γ_c, four distinct dynamic adhesion states, namely, rolling, tumbling, firm adhesion, and detachment, are observed. Before more delicate investigation into the dynamical characteristics (e.g., migration velocity, deformation degree, and bond number), simulation snapshots and motion characteristics of the cell pair are first illustrated in Figs. 2–6 to demonstrate the four adhesion states. For ease of description, we name the cell initially put in the downstream as the *front cell*, and the initially upstream cell as the *rear cell*. Two triangular elements on the membranes are marked in green and red for the *front cell* and the *rear cell*, respectively, as tracers to illustrate the cell motion.

The parametric settings in Fig. 2, i.e., Ca = 0.002, $\Gamma_s =$ 50, and $\Gamma_c = 50$, represent the case with small deformability and weak cell-substrate and cell-cell adhesion strengths. In such adhesion condition, rolling adhesion of the cell pair is observed. Driven by hydrodynamic force from the shear flow, the two cells are slightly deformed and keep rolling along the substrate. Bonds at the trailing edge of each cell are highly stretched, providing pulling forces to counterbalance the hydrodynamic force before their breakage. Meanwhile, new bonds are continually formed at the leading edge with the rotation of the cell. It is worth noting that although only a few bonds at the periphery of the contact region provide main pulling forces, the unstressed bonds (length less than λ) at the center contribute to quickly filling up the load-bearing bonds after bond breakage and thus maintain the rolling motion. Similar physics was also observed by Khismatullin and Truskey [39] and Zhang *et al.* [27] for the rolling adhesion of a single cell. Once the balance between the association and dissociation of bonds is achieved, stable rolling motion can be established. Under such state, the dynamical characteristics of the *front cell* (see Fig. 6), such as the linked bonds and the migration velocity, generally remains constant, although minor fluctuations caused by the binding kinetics exist.

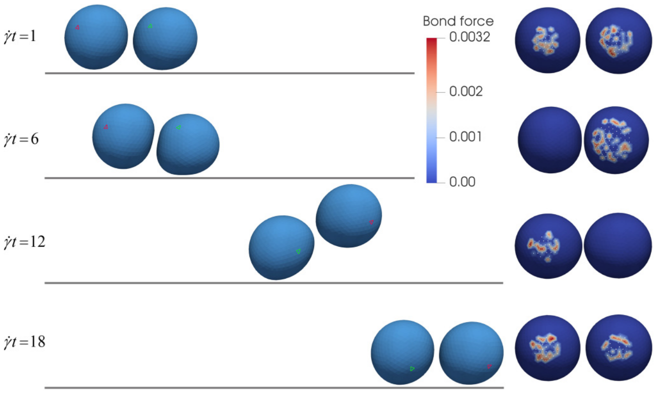

FIG. 3. Simulation snapshots of a cell pair presenting the tumbling adhesion state at Ca = 0.002, $\Gamma_s = 50$, and $\Gamma_c = 150$.

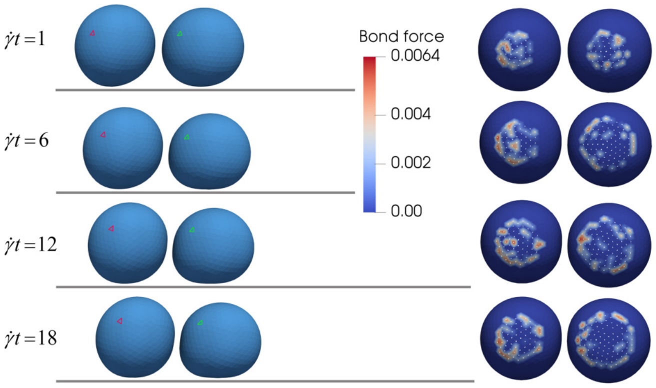

FIG. 4. Simulation snapshots of a cell pair presenting the firm-adhesion state at Ca = 0.002, $\Gamma_s = 100$, and $\Gamma_c = 150$.

The small value of Γ_c indicates weak intercellular binding, which triggers the relative rotation of the two cells. By increasing the intercellular adhesion strength up to 150, the relative rotation vanishes and the cell pair reaches the tumbling state (Fig. 3). The strengthened bonds between the two cells not only give rise to larger resistance to rolling, but

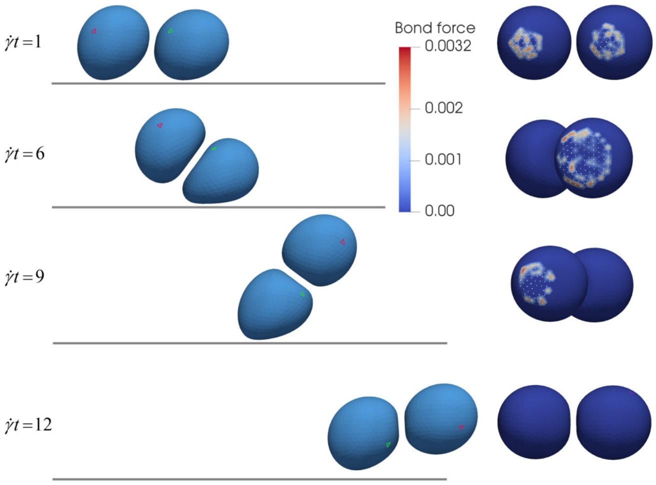

FIG. 5. Simulation snapshots of a cell pair presenting the detachment state at Ca = 0.008, $\Gamma_s = 50$, and $\Gamma_c = 150$.

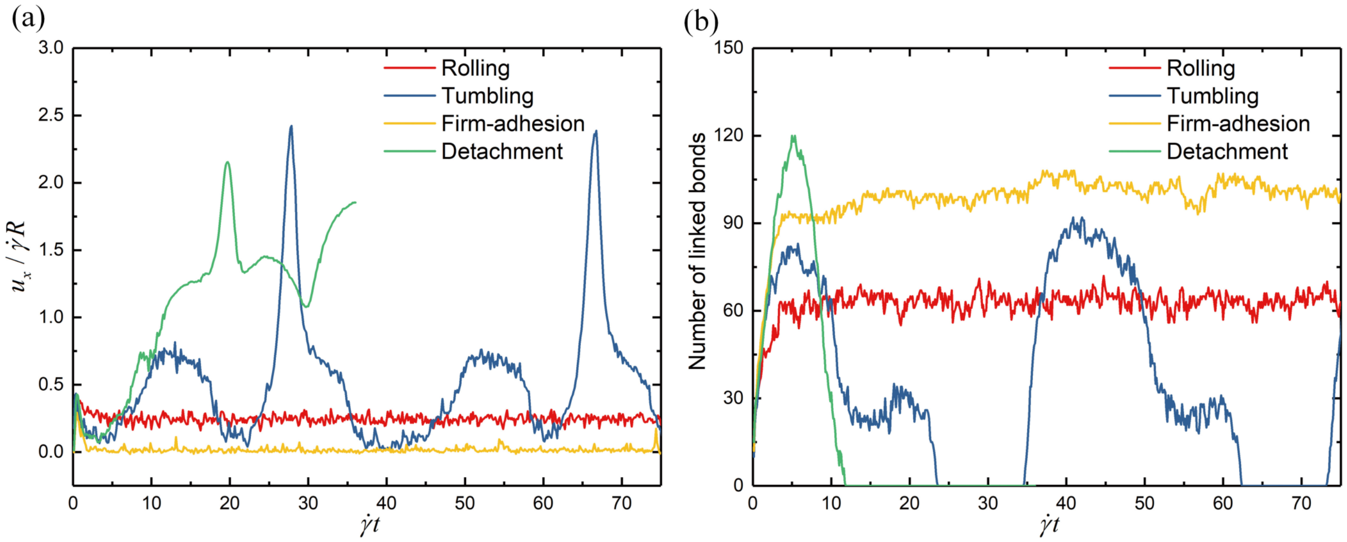

FIG. 6. Time histories of (a) the translational velocity of the *front cell* and (b) the number of linked bonds on its bottom, for the four distinct cases shown in Figs. 2–5.

also stimulate the deformation of the cells. Consequently, the hydrodynamic force acting on the cell pair makes the *rear cell* break away from the substrate and raises it over the *front cell*. A dramatic increase in the migration velocity could be observed due to the detachment (as seen in Fig. 6). The lifted cell will roll over the lower cell and attach the substrate again, after which another circle of tumbling commences and the periodic tumbling state forms.

By strengthening the adhesion between the cell and the substrate to $\Gamma_s = 100$, as in Fig. 4, the cell is largely flattened at the bottom by the bond force, which in turn induces more bonds to be formed. As a consequence, the two cells are firmly attached to the substrate by the pulling forces from the bonds on the bottom and between the cells, and the firm-adhesion state is achieved. On the contrary, by reducing the cell-substrate adhesion strength and enlarging cell deformability ($\mathrm{Ca} = 0.008$, $\Gamma_s = 50$, as in Fig. 5), the bonds do not have sufficient strength to sustain the hydrodynamic load exerted by the flowing fluid. The *rear cell* first detaches from the substrate and leads to the detachment of the whole cell pair. It should be noted that, in some cases with small intercellular binding force, one cell detaches from both the substrate and the other cell. Although this is different from the motion in Fig. 5, we also regard these cases as the detachment state.

B. Phase diagrams for the adhesion dynamics

The numerical examples shown in the previous subsection indicate strong dependence of adhesion states of the cell pair on the adhesion strengths and cell deformability. Physiologically, the capillary number is ranging from 1×10^{-4} to 5×10^{-3} for leukocytes rolling [14,26]; the receptor-ligand bond that mediates cell adhesion is also varied in the adhesion strength, which was measured for single P-, E-, and L-selectin bonds and was estimated to be in the range of 37–250 pN [57]. To further investigate how motion states of the cell pair are affected by these properties, phase diagrams in the space of the intercellular and cell-substrate adhesion strengths with different cell deformability are established and shown in Fig. 7. The capillary number is varied from 0.001 to 0.008; Γ_c is from 0 to 250, and Γ_s varies from 25 to 200. All the four adhesion states can be identified in the phase diagrams. It is noteworthy that a single cell was predicted to present rolling adhesion within the range of parameters, whereas the presence of the second cell significantly changes the adhesive dynamics.

For ease of description, the rolling and firm-adhesion states are labeled as regions I and III, respectively; the tumbling and detachment states are labeled as region II since both the adhesion states are characterized by the detachment of the *rear cell*. The cell pairs that present a stop-and-go motion or exhibit inconsistent adhesion states in different simulation runs are considered as the transition state that partitions the regions (dashed lines). As a general observation in the phase diagrams, cell pairs with weak cell-cell interactions (Γ_c) and small deformability (Ca) are more prone to rolling, and increases in the intercellular adhesion strength would lead to firm adhesion at strong cell-to-wall adhesion and tumbling or detaching at small Γ_s.

In particular, for the most rigid membrane [i.e., $\mathrm{Ca} = 0.001$ in Fig. 7(a)], both the cells are hardly deformed, maintaining the spherical shape which is conducive to rolling. Even with the adhesion strength up to $\Gamma_s = 200$, the cell pair could present rolling adhesion as Γ_c is very small ($\leqslant 50$). Nevertheless, larger intercellular adhesion strength ($\Gamma_c \geqslant 100$) strengthens the bonding between cells and thus impedes the rolling motion. As a result, the motion of the cell pair receiving large bonding forces from the substrate transforms into the firm-adhesion state. It is observed that the critical value of Γ_s for the roll-to-firm (I-III) transition decreases with the increase of Γ_c, which indicates that firm adhesion of the cell pair is facilitated by the adhesive force between the cells. In contrast, for weak cell-substrate adhesion strength ($\Gamma_s < 50$), the *rear cell* is lifted up by the hydrodynamic force, ending up in detachment or tumbling. It can be noted that only in a certain parameter case, i.e., $\Gamma_c = 100$ and $\Gamma_s = 25$, does

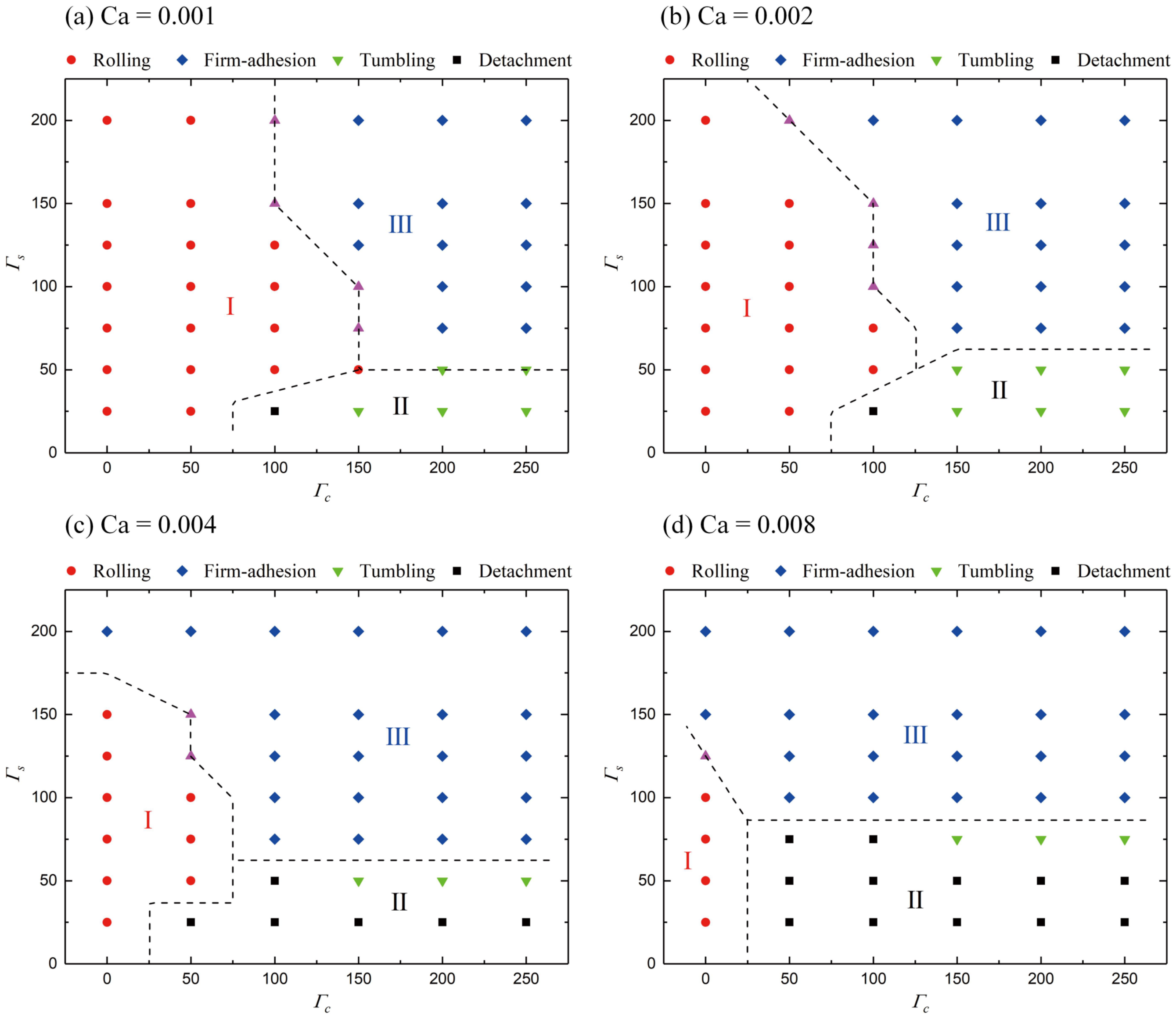

FIG. 7. Adhesion phase diagrams of the cell pair as a function of cell-cell and cell-substrate adhesion strengths with various capillary numbers (Ca = 0.001–0.008). Stop-and-go adhesion is defined as a transition state, marked with the upper triangular.

the cell pair exhibit a detachment state. This is the case that the *rear cell* detaches from both the wall and the other cell, while the *front cell* still rolls on the substrate. Nevertheless, as Γ_c increases to 150, the intercellular adhesive force is strong enough to bind the two cells and contributes to the detachment of the rolling *front cell*. Then after the rollover, the cells could still interact with the substrate alternately, resulting in the tumbling state.

Although slightly increasing the capillary number to 0.002 enlarges regions II and III and shrinks the rolling region, no essential change in the borderline among the state regions is spotted by comparing Fig. 7(b) with Fig. 7(a). Besides, it is noted that the cell pairs can no longer exhibit a stable rolling adhesion state when $\Gamma_c \geqslant 150$. Under such strong intercellular adhesion, the two cells are firmly bonded as a whole. Self-rotation is thus obstructed and the cell pair is more likely to move in the tumbling or firm-adhesion state. Moreover, as the cells become more compliant, the effect of intercellular interaction is more prominent. It is observed in Figs. 7(c) and 7(d) that the rolling region (I) is extremely narrowed at Ca = 0.004, and it even vanishes at Ca = 0.008 unless intercellular adhesive force is removed. The reason is that the more flattened intercellular contact surface under large Ca contributes to forming more adhesion bonds and thus suppresses the rolling of the individual cells (see Fig. 5). In such circumstances, smaller Γ_c is expected for the transitions of rolling to detachment and rolling to firm adhesion. Accordingly, both region II and region III are expanded towards smaller Γ_c by increasing the capillary number. The observation implies that the increase in cell deformability not only promotes firm adhesion, but also facilitates detachment of the cell pair if the adhesion strength Γ_s is below a certain value. Moreover, it is noted that region II even extends towards larger Γ_s for Ca = 0.008, indicating that cell detachment is more favored by increasing the deformability. On one hand, the more deformed *rear cell* has a larger cross section and

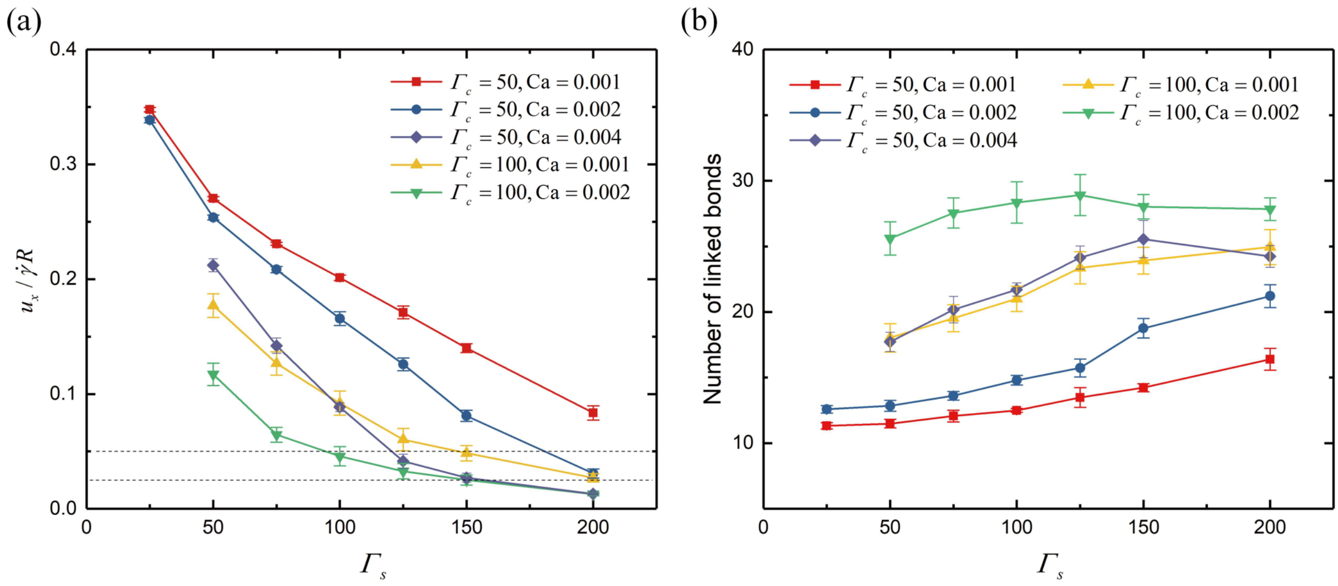

FIG. 8. (a) Average translational velocity of the *front cell* and (b) average number of the linked bonds between the two cells. The mean value and standard error are collected from six independent simulation runs for each case.

is thus subject to a larger torque and drag force. On the other hand, the cell with large capillary number could be quickly deformed to a tilt-teardrop shape with only a few bonds linked at the trailing edge (see Fig. 5), which facilitates its detachment from the substrate. Therefore, larger Γ_s is necessary for the more compliant cell pair to achieve firm attachment or to maintain the tumbling state.

C. Dynamical characteristics of the cell pair

In the above sections, the motions of the cell pair have been classified into four adhesion states as shown in the phase diagrams. However, detailed dynamical characteristics of the aggregate in the same adhesion state could be dependent on the various cell deformability and adhesion strengths. In this section, we will investigate their effects on the variation of the velocity, bond number, and cell deformation.

As can be observed in Fig. 6, the rolling and firm-adhesion cell pairs reach a quasisteady state after the initial transient evolution. The motion characteristics of the quasisteady state under different parametric settings are reported below for comparison. The average translational velocity of the *front cell* (almost the same as the *rear* one) and the average number of intercellular bonds are shown as a function of cell-substrate adhesion strength in Fig. 8. It is noted that the velocities ($u_x/\dot{\gamma}R$) of the cases in the firm-adhesion state fall below 0.025, while the velocities of the cases in the transition state are between 0.025 and 0.05 (dashed straight lines). These characteristics can be used to identify the specific adhesion states. A general discipline observed in Fig. 8(a) is that cell migration velocity decreases with the increase of the cell-substrate adhesion strength. Besides, the cell pairs with larger capillary numbers are more affected by the bond force, presenting a slower migration and more rapid decrease in the velocity with rising Γ_s. Therefore, the transition from rolling to firm adhesion occurs at smaller Γ_s for the more compliant aggregates.

The correlation between the intercellular adhesion strength and migration velocity is reflected as the sharp decrease of the velocity when Γ_c reaches 100, as presented in Fig. 8(a). When we see the number of intercellular bonds in Fig. 8(b), it is interesting to note that its variations with the parameters are opposite but similar to the migration velocity, which indicates the importance of cell-cell interaction in affecting the rolling of the cell pair. Larger capillary number stimulates the deformation, which enlarges intercellular contact area and constructs more bonds. With further increased Γ_c, the cells are not only more deformed, but also linked with stronger bonds. Accordingly, cell pairs with larger deformability and intercellular adhesion strength have more linked bonds, which in turn provide more resistance against the rolling.

Figure 9 presents the number of linked bonds between the cells and the substrate in different cases. It is found that the number of cell-substrate bonds is more sensitive to the cell deformability and the cell-substrate adhesion strength than to the intercellular adhesion strength. At small adhesion strength ($\Gamma_s \leqslant 50$), the *rear cells* with different capillary numbers almost have the same number of linked bonds. Deviations start with the increase in Γ_s as the bond number increases more rapidly for more compliant cells. A similar trend for the *front cell* can be observed, except that the *front cell* has more linking bonds than the rear one during the rolling. Under the forces from the shear flow and the intercellular bonds, the *front cell* is pushed downwards, increasing bond formation while the *rear cell* is lifted upwards (see Fig. 4).

Cell deformation is quantified by the deformation parameter defined as $D = (r_{\max} - r_{\min})/(r_{\max} + r_{\min})$, where $r_{\max}$ and $r_{\min}$ are the longest and shortest distances between the cell centroid and the membrane, respectively. Figure 10 illustrates the deformation parameters of the two cells in different cases. As expected, cell deformation increases with the cell-substrate

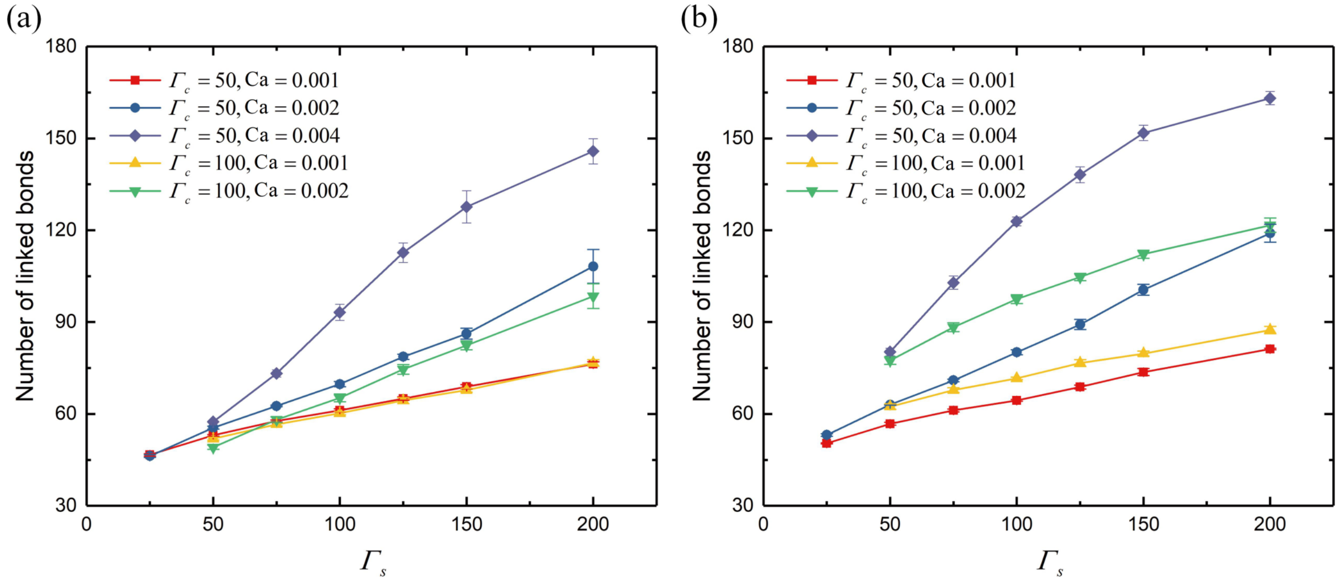

FIG. 9. Average number of linked bonds on the bottom of (a) the *rear cell* and (b) the *front cell* (mean±SE; $n = 6$).

adhesion strength, and steeper increases are found for the cell pair with larger capillary numbers. It is noted that the deformation of the *front cell* is also slightly increased by increasing the intercellular adhesion strength to 100, whereas a minor decrease in the deformation of the *rear cell* is observed, owing to the vertical deformation imposed by the intercellular force. Since cell deformability has a major effect on cell-wall contact area, the variation of bond number with Γ_s is similar to the variation of the deformation parameter when comparing Figs. 9 and 10. However, it is worth noting that although the *rear cell* has nearly the same number of bonds linked at the bottom when Γ_s is small ($\leqslant 50$), it is featured by different degrees of deformation for varied capillary numbers. This indicates that the *rear cell*, at the rolling state, is deformed in a way that the forepart is lifted and only a small part of the bottom at the tail is bonded to the substrate. It is because of such form of rolling that either increasing the deformability or reducing the cell-substrate adhesion strength could give rise to the roll-to-detach transition of the *rear cell*.

The detaching of the *rear cell* from the substrate will finally lead to the detachment or tumbling states of the cell pair. In the detachment state, the aggregate freely flows with the ambient fluid and gradually moves far away from the substrate. The detachment state is not further studied in this work, since dynamical characteristics of aggregated cells or capsules in shear flows can be found in previous studies [36,58]. For cell pairs reaching the tumbling state, the tumbling pattern is recurring during the adhesion motion as seen in Fig. 6. In the following, the dynamical characteristics of the periodic motion are compared.

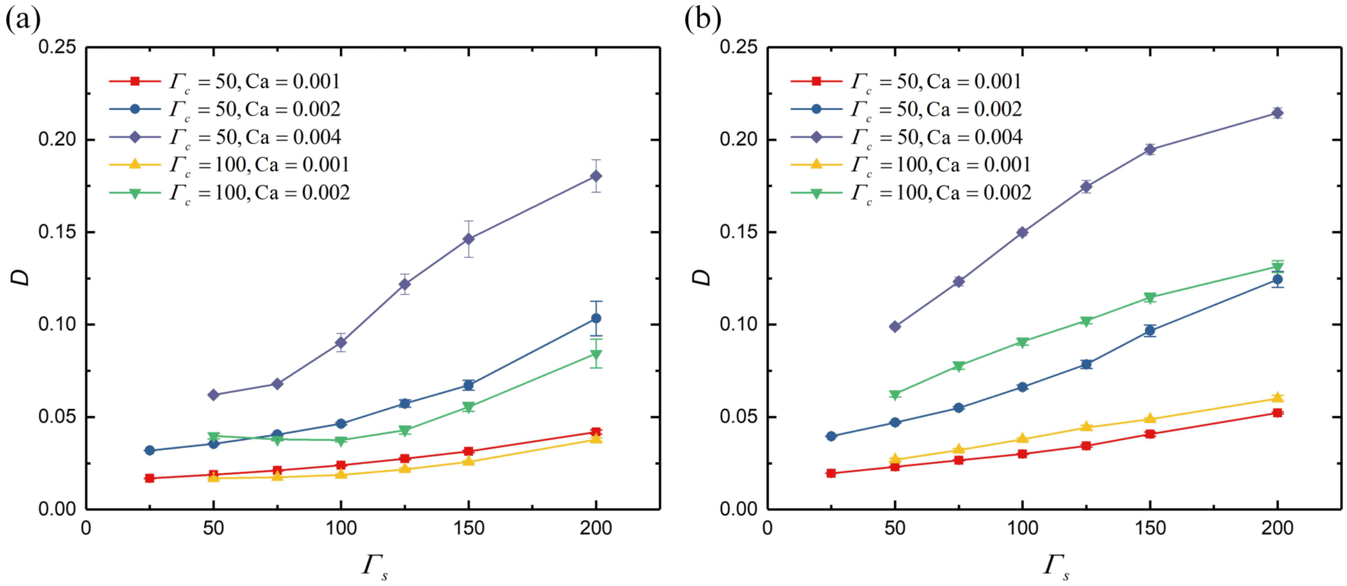

FIG. 10. Average deformation of (a) the *rear cell* and (b) the *front cell* (mean±SE; $n = 6$).

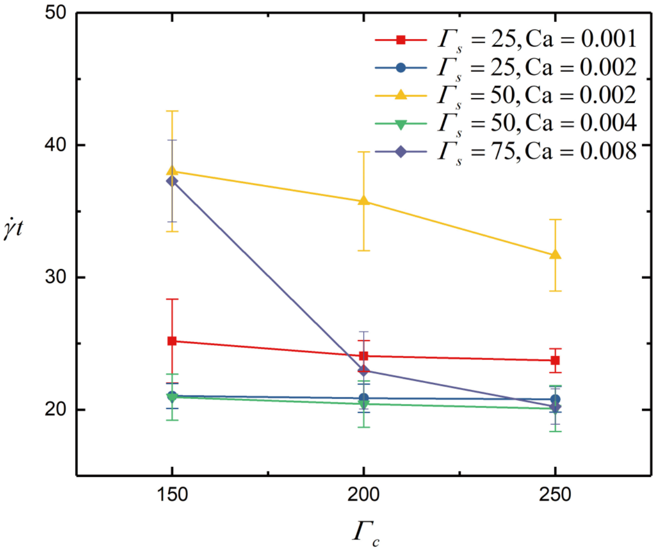

FIG. 11. Average period of a tumbling motion (mean±SE; $n = 6$).

The period of a complete tumbling motion, defined as the time period between two sequential detachments of the *rear cell*, is reported in Fig. 11. During a period, the *rear cell* detached, tumbled, and bonded with the substrate; then after tumbling the other one, the *rear cell* detached again. A smaller period indicates faster tumbling of the cell pair on the substrate, which is observed in cases with larger cell deformability for the same Γ_s. It is noted that certain tumbling cases (i.e., $\mathrm{Ca} = 0.002$ with $\Gamma_s = 50$, and $\mathrm{Ca} = 0.008$ with $\Gamma_s = 75$ and $\Gamma_c = 150$) present a much larger period than others. This is owing to the particular cell-substrate adhesion strength that provides just enough resistance to delay the detachment of the *front cell* after rolling over and maintains a short interval during which both cells bind to the substrate again (i.e., Fig. 3), whereas in other tumbling cases only one cell interacts with the substrate at the same time. This particular pattern of tumbling also leads to the observation that increasing Γ_c clearly shortens the period of the particular tumbling cases but rarely has effects on the others, since the intercellular binding force could promote the detachment of the upstream cell when both cells are adhering to the substrate.

During the tumbling motion, the cell pair is repeatedly pressed and stretched by the shear flow, resulting in varying numbers of linked bonds between the two cells. The average minimum and maximum numbers of intercellular bonds are shown in Fig. 12 to further compare the intercellular interactions of the cell pair during tumbling. The maximum number of intercellular bonds appears when one cell starts to roll over the other one (e.g., Fig. 3 $\dot{\gamma}t = 6$), which also reveals the maximum contact area for the intercellular interactions. After the rollover, the minimum bond number appears when one cell is still adhering to the substrate but the other one tends to drift downstream (e.g., Fig. 3 $\dot{\gamma}t = 12$). With the number of bonds linked, the bonds are able to persist long enough with sufficient strength to keep the aggregate from breaking apart.

For cases with $\mathrm{Ca} = 0.001$ and 0.002, the intercellular adhesion strength shows little influence on the linked bonds: only a slight increase in the bond number is observed by increasing Γ_c. It implies that within this range of Γ_c, the variation of the contact area of the tumbling cell pair is mainly enforced by the hydrodynamic force. As for cases with $\mathrm{Ca} = 0.004$, however, the linked bonds are pronouncedly increased by increasing Γ_c, especially the minimum bonds. A similar variation trend is also observed in cases with $\mathrm{Ca} = 0.008$, but with nearly double the number of linked bonds (not shown). Such soft cells can be more easily deformed by the bond force and the compliant membrane is not able to provide sufficient force to break the bonds. Thus, the influence of Γ_c on the intercellular interaction becomes significant as $\mathrm{Ca} \geqslant 0.004$. In addition, it is noted that increases in either Γ_s or Ca can enlarge the contact area and thus increase the maximum number of bonds, while the minimum number of bonds is rarely affected when the deformability is small ($\mathrm{Ca} \leqslant 0.002$).

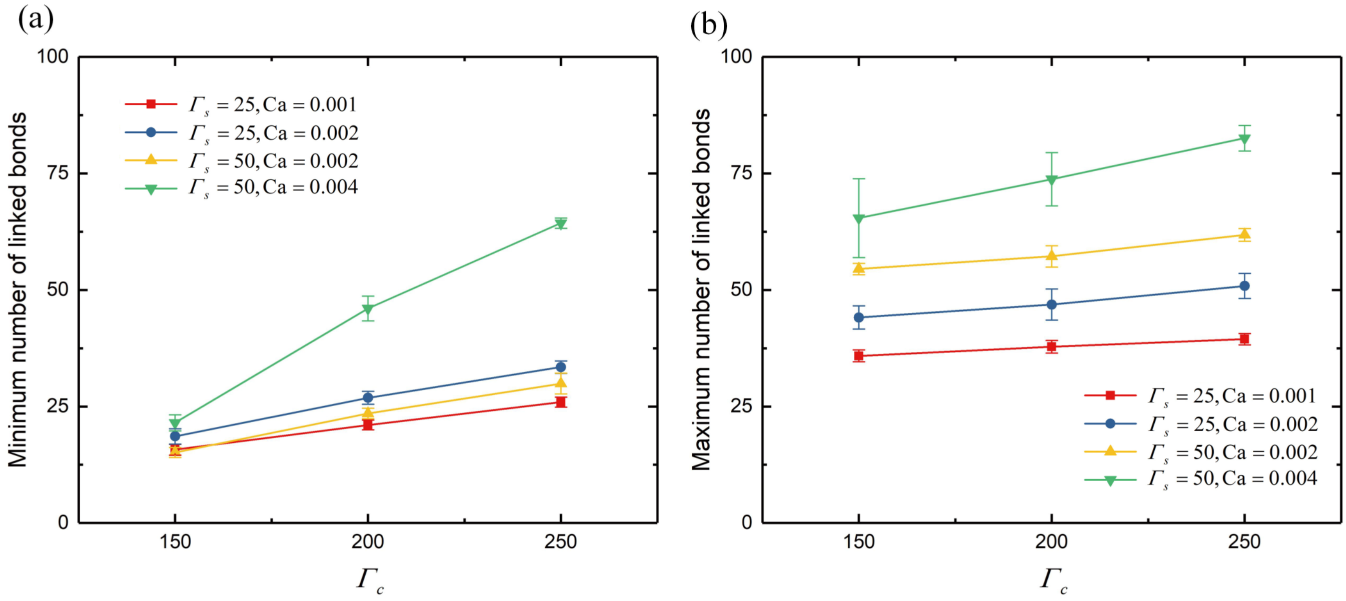

FIG. 12. Minimum and maximum numbers of linked bonds between the two cells during the tumbling motion (mean±SE; $n = 6$).

IV. CONCLUSIONS

The adhesion dynamics of an aggregate of two cells under linear shear flow has been numerically investigated in this paper. The cell pair could orchestrate into four adhesion states, namely, rolling, tumbling, firm adhesion, and detachment, dictated by the competition among cell-cell and cell-substrate adhesion strengths (quantified by Γ_c and Γ_s) and cell deformability (quantified by Ca). Phase diagrams are established to reveal the association between the motion behavior and these parameters. Specifically, weaker intercellular adhesion strength and smaller deformability would favor the rolling motion of the cell pair. The stronger cell-cell adhesion would increase the number of intercellular bonds and thus hinder the rolling motion, and could transfer either towards the firm-adhesion state with sufficiently strong cell-substrate adhesion, or towards the tumbling or the detachment state by reducing Γ_s. The cell deformability also casts significant influence on the adhesion dynamics of the cell pair. On one hand, the increase of cell deformability could strengthen adhesive binding between the surfaces by enlarging contact area and increasing the number of bonds, which hinders the rolling motion and expands the firm-adhesion region. On the other hand, under weak cell-substrate adhesion strength, larger cell deformability could facilitate the detachment or tumbling motion due to the tilt-teardrop shape.

It is noteworthy that the adhesion behaviors of the cell pair clearly differ from that of the individual cells. Within the parameter space of the phase diagrams presented in this paper, a single cell would only present rolling adhesion under the shear flow. The presence of another cell brings in intercellular interactions and thus complicates the adhesion dynamics. The results could contribute to further understanding of similar physiological problems. For instance, the established phase diagrams may provide an explanation in the physical aspect for why tumor cell clusters exhibit much higher metastatic capacity. As compared with the single cell, an aggregate is more likely to detach or tumble under large flow rates (i.e., small Γ_s) and then rapidly spread with the bloodstream; at distant sites with small flow rates or abundant ligands possessing large Γ_s, the tumor cell aggregate could firmly adhere to the vascular endothelium which is a prerequisite of the metastatic process. Thus, if the intercellular adhesion of tumor cells is inhibited (i.e., to decrease Γ_c), for example, by plakoglobin knockdown, metastases would be suppressed [30]. Additionally, the adhesive characteristics of cell aggregates also contribute to the understanding of other diseases, such as platelet aggregation in thrombosis [59], and in severe malaria, RBC aggregates adhering to the endothelium to escape splenic clearance [60]. As can be inferred from the phase diagrams, the prevention of the firm adhesion of the aggregate can be achieved by either weakening the cell-cell and cell-vessel adhesion to keep it in the rolling region or softening the cells to facilitate the detachment.

It should be noted that the number of repeated runs for each case may not be statistically significant. Certain variations of the simulation results may show up if increasing the number of runs. Furthermore, the system only considered an ideal scenario wherein the cells were arranged as a chain in parallel with the shear flow, and changes in the chain-flow angle could radically alter the adhesion dynamics. We also note that some other factors, such as the on and off reaction rates of the bond, the presence of a nucleus, and a larger cell cluster, which would affect the adhesion behaviors in a crucial way, should be further investigated.

ACKNOWLEDGMENTS

This work was funded by the National Natural Science Foundation of China (Grants No. 31370944 and No. 51775420). Z.Z. gratefully acknowledges financial support from the China Scholarship Council.

---

[1] D. N. Granger and P. Kubes, J. Leukocyte Biol. **55**, 662 (1994).
[2] Z. M. Ruggeri, J. A. Dent, and E. Saldívar, Blood **94**, 172 (1999).
[3] J. M. Karp and G. S. Leng Teo, Cell Stem Cell **4**, 206 (2009).
[4] W. C. Chang, L. P. Lee, and D. Liepmann, Lab Chip **5**, 64 (2005).
[5] T. F. Didar and M. Tabrizian, Lab Chip **10**, 3043 (2010).
[6] A. K. Dasanna and U. S. Schwarz, Soft Matter **14**, 9061 (2018).
[7] A. A. Khalili and M. R. Ahmad, Int. J. Mol. Sci. **16**, 18149 (2015).
[8] D. A. Hammer, J. Biomech. Eng. **136**, 021006 (2014).
[9] D. A. Fedosov, W. Pan, B. Caswell, G. Gompper, and G. E. Karniadakis, Proc. Natl. Acad. Sci. USA **108**, 11772 (2011).
[10] A. Alexeev, R. Verberg, and A. C. Balazs, Soft Matter **2**, 499 (2006).
[11] D. B. Khismatullin and G. A. Truskey, Phys. Fluids **17**, 031505 (2005).
[12] Z. Y. Luo and B. F. Bai, Soft Matter **12**, 6918 (2016).
[13] D. A. Hammer and S. M. Apte, Biophys. J. **63**, 35 (1992).
[14] S. Jadhav, C. D. Eggleton, and K. Konstantopoulos, Biophys. J. **88**, 96 (2005).
[15] W. Wang, N. A. Mody, and M. R. King, J. Comput. Phys. **244**, 223 (2013).
[16] X. Zheng, L. S. Cheung, J. A. Schroeder, L. Jiang, and Y. Zohar, Lab Chip **11**, 3431 (2011).
[17] H. D. Balsara, R. J. Banton, and C. D. Eggleton, Biomech. Model. Mechanobiol. **15**, 1055 (2016).
[18] M. J. Paszek, D. Boettiger, V. M. Weaver, and D. A. Hammer, PLoS Comput. Biol. **5**, e1000604 (2009).
[19] D. A. Fedosov, B. Caswell, and G. E. Karniadakis, Biophys. J. **100**, 2084 (2011).
[20] K. C. Chang, D. F. Tees, and D. A. Hammer, Proc. Natl. Acad. Sci. USA **97**, 11262 (2000).
[21] S. K. Bhatia, M. R. King, and D. A. Hammer, Biophys. J. **84**, 2671 (2003).
[22] C. B. Korn and U. S. Schwarz, Phys. Rev. E **77**, 041904 (2008).
[23] F. Y. Leong and K. H. Chiam, Phys. Rev. E **81**, 041923 (2010).
[24] A. Carlson and L. Mahadevan, PLoS Comput. Biol. **11**, e1004481 (2015).

[25] K. Liu, B. Chu, J. Newby, E. L. Read, J. Lowengrub, and J. Allard, PLoS Comput. Biol. **15**, e1006352 (2019).
[26] V. Pappu and P. Bagchi, Comput. Biol. Med. **38**, 738 (2008).
[27] Z. Zhang, J. Du, Z. Wei, Z. Wang, and M. Li, Biomech. Model. Mechanobiol. **17**, 223 (2018).
[28] A. K. Dasanna, C. Lansche, M. Lanzer, and U. S. Schwarz, Biophys. J. **112**, 1908 (2017).
[29] L. A. Liotta, J. Kleinerman, and G. M. Saldel, Cancer Res. **36**, 889 (1976).
[30] N. Aceto *et al.*, Cell **158**, 1110 (2014).
[31] S. Jadhav, K. Y. Chan, K. Konstantopoulos, and C. D. Eggleton, J. Biomech. **40**, 2891 (2007).
[32] E. Lac, A. Morel, and D. Barthès-Biesel, J. Fluid Mech. **573**, 149 (2007).
[33] S. K. Doddi and P. Bagchi, Int. J. Multiphase Flow **34**, 375 (2008).
[34] H. Lan and D. B. Khismatullin, Phys. Rev. E **90**, 012705 (2014).
[35] M. R. King and D. A. Hammer, Biophys. J. **81**, 799 (2001).
[36] J. Zhang, P. C. Johnson, and A. S. Popel, J. Biomech. **41**, 47 (2008).
[37] V. K. Gupta, I. A. Sraj, K. Konstantopoulos, and C. D. Eggleton, Biomech. Model. Mechanobiol. **9**, 613 (2010).
[38] T. Krüger, Comput. Math. Appl. **61**, 3485 (2011).
[39] D. B. Khismatullin and G. A. Truskey, Biophys. J. **102**, 1757 (2012).
[40] C. Korn and U. S. Schwarz, Phys. Rev. Lett. **97**, 138103 (2006).
[41] Z. Zhang, J. Du, Z. Wei, Z. Wang, H. Zhang, M. Li, and Y. Tang, Comput. Math. Appl. (2018), doi: 10.1016/j.camwa.2018.01.027.
[42] D. D'Humieres, I. Ginzburg, M. Krafczyk, P. Lallemand, and L. S. Luo, Philos Trans. R. Soc., A **360**, 437 (2002).
[43] Z. Guo and C. Shu, *Lattice Boltzmann Method and its Applications in Engineering* (World Scientific, Singapore, 2013), Vol. 3.
[44] A. Ladd and R. Verberg, J. Stat. Phys. **104**, 1191 (2001).
[45] C. S. Peskin, Acta Numer. **11**, 479 (2003).
[46] S. Ramanujan and C. Pozrikidis, J. Fluid Mech. **361**, 117 (1998).
[47] T. Krüger, M. Gross, D. Raabe, and F. Varnik, Soft Matter **9**, 9008 (2013).
[48] D. Barthès-Biesel, A. Diaz, and E. Dhenin, J. Fluid Mech. **460**, 211 (2002).
[49] A. Yazdani and P. Bagchi, J. Fluid Mech. **718**, 569 (2013).
[50] M. Dembo, D. C. Torney, K. Saxman, and D. Hammer, Proc. R. Soc. B **234**, 55 (1988).
[51] G. I. Bell, M. Dembo, and P. Bongrand, Biophys. J. **45**, 1051 (1984).
[52] B. T. Marshall, M. Long, J. W. Piper, T. Yago, R. P. McEver, and C. Zhu, Nature **423**, 190 (2003).
[53] N. Q. Nguyen and A. J. Ladd, Phys. Rev. E **66**, 046708 (2002).
[54] S. Chen and T. A. Springer, J. Cell Biol. **144**, 185 (1999).
[55] R. Alon, D. A. Hammer, and T. A. Springer, Nature **374**, 539 (1995).
[56] J. Fritz, A. G. Katopodis, F. Kolbinger, and D. Anselmetti, Proc. Natl. Acad. Sci. USA **95**, 12283 (1998).
[57] M. J. Smith, E. L. Berg, and M. B. Lawrence, Biophys. J. **77**, 3371 (1999).
[58] P. Bagchi, J. Biomech. Eng. **127**, 1070 (2005).
[59] S. P. Jackson, Blood **109**, 5087 (2007).
[60] Q. Chen, M. Schlichtherle, and M. Wahlgren, Clin. Microbiol. Rev. **13**, 439 (2000).